Article

Research on Cavitation Wake Vortex Structures Near the Impeller Tip of a Water-Jet Pump

Yun Long [1,*], Mingyu Zhang [1], Zhen Zhou [1], Jinqing Zhong [1], Ce An [1], Yong Chen [2], Churui Wan [3] and Rongsheng Zhu [1]

1   National Research Center of Pumps, Jiangsu University, Zhenjiang 212013, China
2   State Key Laboratory of Mechanical System and Vibration, Shanghai Jiao Tong University, Shanghai 200240, China
3   Marine Design and Research Institute of China, NO 1688 South Xizang Road, Shanghai 200011, China
*   Correspondence: longyun@ujs.edu.cn

Abstract: Cavitation can cause noise in the water-jet pump. If cavitation occurs in the water-jet pump, the hydraulic components in the pump are prone to erosion. The surface erosion reduces energy delivery efficiency and increases maintenance costs. The decline in pump performance will lead to the instability of the entire energy system. In this paper, the cavitation flow structure of the water-jet pump is studied by the method of numerical simulation and experiment, which provides a reference for the prediction and improvement of cavitation. Based on the closed test platform, in order to reveal the physical process of cavitation evolution, high-speed photography is used to capture the complex cavitation flow phenomenon in the pump. After that, the cavitation vortex structure was further explored by numerical simulation. Through the simulation of the impeller blade tip leakage flow and the Tip Leakage Vortex Cavitation (TLVC) characteristics under different cavitation conditions, the flow mechanism of the impeller blade tip leakage flow and the separation vortex induced by the cavitation region under different cavitation conditions were revealed. The main factors affecting the development of the cavitation wake vortex structures were summarized.

Keywords: water-jet pump; cavitation; cavitation flow structure

1. Introduction

The key to the development of the water-jet pump is research on the high efficiency and high anti-cavitation performance of pumps. Typically, water-jet pumps are designed to ensure high efficiency at high-speeds through optimization of the impeller and diffuser while meeting special requirements, such as strong anti-cavitation resistance and low vibration and noise. PEI Ji et al. [1] optimized the centrifugal pump impeller through the orthogonal DOE, used CFD to evaluate several key geometric parameters of the impeller, and set up an open test rig for test verification. Finally, the impeller with improved cavitation performance under the premise of ensuring efficiency was obtained.

When cavitation occurs in the water-jet pump, the thrust will be reduced. Furthermore, the efficiency will decrease and the noise will increase rapidly. When the water-jet pump is run under cavitation conditions for a long time, cavitation erosion of hydraulic components will also be caused. The surface erosion of the hydraulic component requires serious suspension repair or component replacement, so the energy transfer efficiency is reduced and the maintenance cost of the equipment is increased. The decline in pump performance will lead to instability throughout the entire energy system. Based on the above reasons, it is significant to carry out research on improving the anti-cavitation performance of the pump [2,3].

The cavitation phenomenon mainly includes large-scale vortices in the vapor and liquid phases and the process of phase transition. Cheng-zao Han et al. [4] adopted the LES method combined with the ZGB cavitation model to conduct numerical calculations and

analyses on the tip clearance flow of the propelling pump, and explored the interaction between the cavitation phenomenon and the vortex. They found that most vortices appeared at the cavitation area, and cavitation enhanced the strength of the tip clearance vortices of the pump. Meanwhile, the relative vorticity transport equation is used in the cavitation turbulence, and it is found that the vortex stretching term, the baroclinic torque term, and the dilation term are all important source terms for cavitation vortices. Cavitation flow is a complex, two-phase turbulent flow. There are energy, mass, and momentum exchanges between the vapor phase and the liquid phase. Therefore, more and more scholars pay attention to the accurate capture and monitoring of the cavitation phenomenon, which is generally studied through a combination of experiment and numerical simulation. Delin Li et al. [5] used the DDES numerical calculation method to study the centrifugal pump with a vane diffuser, extracted and analyzed the vortex structure under the vane passing frequency, and captured the horseshoe vortex using the Q-criterion. The study found that the impeller outlet, the trailing edge of the diffuser, and the vicinity of the volute tongue were the main concentration areas of the vortex.

Desheng Zhang et al. [6] obtained images of the evolution process of vortex cavitation in the tip region of an axial-flow pump through high-speed photography and used an improved filter-based model for numerical simulation to explore the characteristics and development mechanism of tip vortex cavitation. Yi Li et al. [7] proposed a STFT-WVD united algorithm to explore the time-frequency characteristics of the cavitation phenomenon, which leads to pump instability, and to better detect the cavitation performance of the pump. Razieh Azizi et al. [8] conducted a vibration analysis of centrifugal pump through a test of visualization, thus achieving the purpose of detecting cavitation phenomena. At the same time, DWT and EMD algorithms are used to extract pump vibration characteristics to monitor pump cavitation. Mingming Ge et al. [9] studied the turbulent cavitation flow in the Venturi's channel using ultra-fast X-ray imaging technology.

In order to improve the adverse consequences of cavitation, scholars have carried out research on the influence of different factors on pump cavitation performance. Jiaxing Lu et al. [10] built a closed test rig and combined the numerical simulation results to determine the cavitation degree of the pump by analyzing the pressure pulsation at the inlet and outlet of the centrifugal pump. It was found that the pressure pulsation at the pump inlet has a strong correlation with cavitation. Meng Liu et al. [11] simulated and analyzed the cavitation phenomenon in the central jet pump through the SBES turbulence model and the ZGB cavitation model and found that the accumulation of cavities would lead to instability of the pump and that the influence of different cavitation intensities on the pump was slightly different. Ahmed Ramadhan Al-Obaidi [12] conducted experiments to investigate the effects of different flow rates and rotating speeds on the cavitation performance of centrifugal pumps and found that large flow rates would lead to cavitation in the pump, and the pump speed was positively correlated with the cavitation of the pump. Weihui Xu et al. [13] mainly studied the influence of blade surface roughness on the cavitation performance of centrifugal pumps through numerical simulation and found that properly reducing the wall roughness was conducive to improving the cavitation characteristics of centrifugal pumps. Mingming Ge et al. [14–17] studied the dynamics and thermodynamic effects of cavitation at different temperatures in the venturi channel through a series of technical means, such as the visualization test, PIV measurement, and DMD and POD decomposition, and clearly displayed the cavitation flow state. It was found that the cavitation length first increased and then decreased with the increase of temperature, reaching the peak of cavitation intensity at 58 °C.

In summary, the existing research focuses on the cavitation two-phase flow mechanism but ignores the cavitation wake vortex structure near the impeller tip. The aim of this paper is to study the characteristics of the cavitation wake vortex structure through a combination of experiments and numerical simulations. The object of the research is the water-jet pump. Based on the high-speed photographic experiments, the effects of the cavitation regions

of the TLV and the impeller suction surface on the cavitation wake vortex structure in different cavitation stages are discussed.

2. Cavitation Test

2.1. High-Speed Photography Acquisition System

To capture the complex flow structures of the pump, many methods could be used. Common measurement techniques for the internal flow of centrifugal pumps include Particle Image Velocimetry (PIV) [18–23], Laser Doppler Velocimetry (LDV) [24,25], and High Speed Photograph (HSP) [26]. PIV is a transient, multi-point, non-contact measurement technology that can capture the velocity information of the whole flow field. It is widely used in various flows, but it has high requirements on test equipment and test conditions. LDV is obtained by the Doppler signal of the tracer particle of the laser probe, and then the velocity is obtained by the relationship between velocity and Doppler frequency. It has the advantages of high measurement accuracy and fast dynamic response. However, when the narrow flow field is measured, the divided beams of LDV are difficult to intersect into measurable states. It has the limitation of a spatial single-point measurement. It is difficult to meet the needs of transient flow field testing. HSP measures the movement of fluid by taking images of high-speed fluid. HSP technology can obtain traces of fluid motion, so the evolution of fluid motion can be obtained [27]. HSP technology has been widely used in the visualization of the cavitation flow morphology and evolution of pumps. Considering the advantages and disadvantages of the above measurement technologies and test conditions, HSP is selected as the main means to capture the flow field in the pump.

In order to observe the cavitation flow state of the impeller, a visualization window is set at the impeller shroud. Figure 1 shows the layout of the test rig for the high-speed photography visualization system of the pump. In order to make the camera capture angle as wide as possible, the elevation formed by the center of gravity of the camera support frame and the camera barrel shaft is aligned with the middle position of the impeller. The distance between the camera lens and the visualization window is about 50 mm, and the size of the shooting area is about 90 mm × 180 mm. The high-speed camera selected in the experiment is PCOS, and the system adopts a fast frame rate of 4467 fps and the resolution of the image (1008 × 1008 pixels), which can produce an excellent test image.
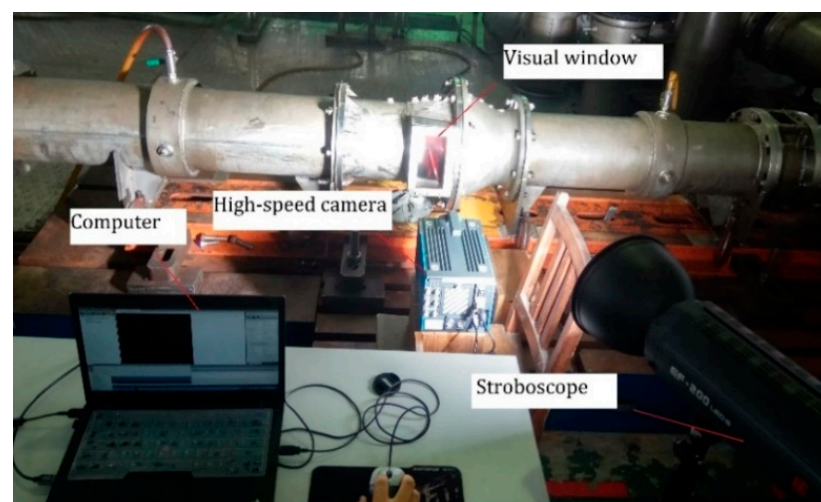
Figure 1. High-speed photography visualization system [28].

In order to better capture the phenomenon of cavitation flow in the pump, it is necessary to determine the shooting frequency of the high-speed camera. If the impeller

speed of the pump is *n*, and the impeller rotates every certain rotation degree α to shoot an image, the shooting frequency *f* is:

$$f = \frac{n \times 360/60}{\alpha} \tag{1}$$

In the formula, *n* is the impeller rotating speed, r/min, and α is the impeller rotation angle, °. In this paper, the high-speed camera is set to shoot an image every 2° rotation of the impeller, and the shooting frequency value is calculated according to Equation (1).

2.2. Water-Jet Pump Model

The design parameters of the water-jet test pump are as follows: flow *Q* is 0.46 m³/s, head *H* is 13 m, rotating speed *n* is 1450 r/min, power *N* is 70 kW, specific speed n_s is 524.3, and impeller inlet diameter D_j is 270 mm.

There are four processes of cavitation: generation, development, critical cavitation, and breakdown cavitation, which can be realized by changing some of the parameters of the pump. The cavitation flow in the pump can be observed through the visualization window. Figure 2 shows the three-dimensional modeling diagram of the pump. Figure 3 shows the physical picture of the model pump.
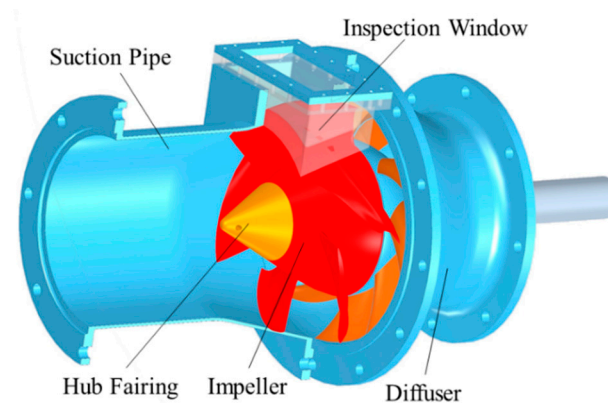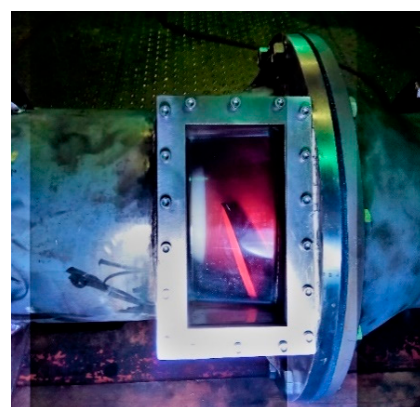

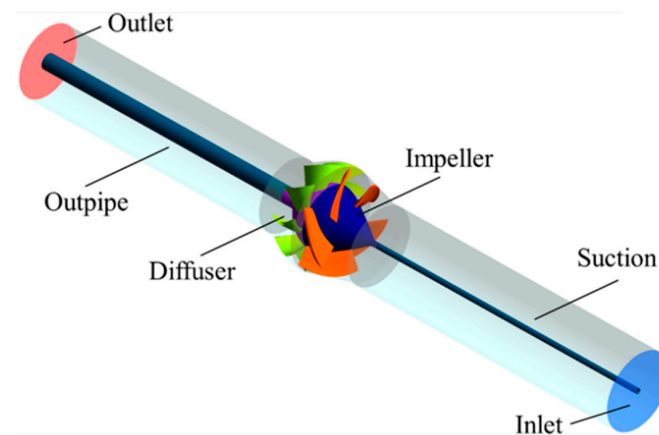**Figure 2.** 3D model of the water-jet pump [3].

| (a) | (b) |

Figure 3. Real hydraulic components of the water-jet pump [3]. (a) Assembly and (b) impeller.

3. Numeral Calculations

3.1. Hydraulic Model Components

Figure 4 shows the domain of hydraulic components, including suction, impeller, diffuser, and outpipe.

Figure 4. Domain of hydraulic components [28].

3.2. Meshing

The calculation model uses the ANSYS-CFX pre-processing gridding software ICEM to perform meshing; structural grids are used on the calculation domain of the suction pipe and outpipe. The impeller and diffuser hydraulic model uses BladeGen to construct the geometric model of the blade and flow passage. The impeller blade has 5 layers, and the leading and trailing edges of the impeller blade are elliptical. The profile of each layer of the blade is fitted with a spline curve. Turbogrid is used to mesh the impeller and the diffuser. In order to accurately predict the cavitation phenomenon in the tip clearance, it is necessary to mesh the tip clearance. Set the gap between the tip clearance of the grid to a nominal distance of 0.3 mm. A 25-layer grid, as shown in Figure 5b, is used to divide the tip clearance region to get a better flow field. In regard to mesh-independent checking, the pump studied in this paper is very similar to Huang Renfang's [29] pump calculation model in geometry dimensions and operation conditions. Huang conducted a mesh independence check on the impeller and indicated that the mesh of the impeller needs to be greater than 1.06 million to ensure calculation performance. The number of grids for each hydraulic component is 1.27 million grids in the impeller, 2.04 million grids in the diffuser, 450,000 grids in the suction pipe, and 370,000 grids in the outpipe. The total number of grid elements is about 4.13 million for all the domains. The assembly of each hydraulic component grid is shown in Figure 5.

(a)
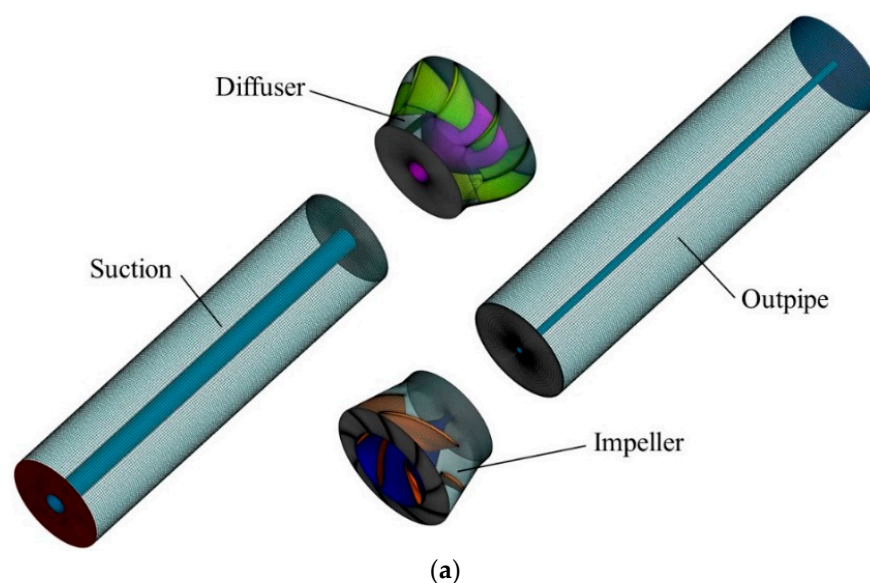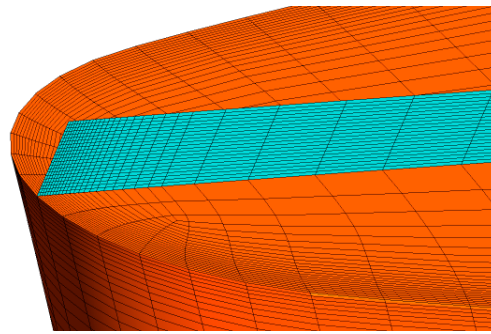
Figure 5. *Cont.*

(b)

Figure 5. The mesh generation. (**a**) Assembly mesh [28]. (**b**) The tip clearance mesh.

3.3. Control Equation

It is assumed that the solution of cavitation flow is uniform flow, that is, multiphase flow composed of liquid and steam is taken as a medium, which means that they have the same velocity and pressure. The continuity equation and momentum equation of the RANS equation are as follows:

$$\frac{\partial \rho_{\mathrm{m}}}{\partial t} + \frac{\partial}{\partial x_j}(\rho_m u_j) = 0 \tag{2}$$

$$\frac{\partial}{\partial t}(\rho_m u_i) + \frac{\partial}{\partial x_j}(\rho_m u_i u_j) = -\frac{\partial p}{\partial x_i} + \frac{\partial}{\partial x_j}\left[(\mu + \mu_t)\left(\frac{\partial u_i}{\partial x_j} + \frac{\partial u_j}{\partial x_i} - \frac{2}{3}\frac{\partial u_k}{\partial x_k}\delta_{ij}\right)\right] \tag{3}$$

where p is the mixing pressure, Pa; u_i is the velocity in the i direction, m/s; μ is the laminar dynamic viscosity, kg/(m·s); and μ_T is the turbulent eddy dynamic viscosity, kg/(m·s). The definition of mixed density ρ_m is as follows:

$$\rho_m = \alpha_v \rho_v + (1 - \alpha_v)\rho_l \tag{4}$$

where the subscripts v and l represent the vapor phase and the liquid phase, respectively. ρ_v stands for vapor density, kg/m^3; ρ_l represents liquid phase density, kg/m^3; and α_v represents the vapor volume fraction.

3.4. Cavitation Model

The cavitation model is evolved from the mass transfer equation to achieve the purpose of converging the volume fraction of the vapor. Its formula is as follows:

$$\frac{\partial \rho_v \alpha_v}{\partial t} + \nabla \cdot (\rho_v \alpha_v u_i) = \dot{m}^+ - \dot{m}^- \tag{5}$$

The source term includes an evaporation term (for example $\dot{m}^+$) and a condensation term (for example $\dot{m}^-$). Zwart [30] gives the following definition:

$$\dot{m}^+ = F_{vap}\frac{3r_{nuc}(1 - \alpha_v)\rho_v}{R_{nuc}}\sqrt{\frac{2}{3}\frac{\max(p_v - p, 0)}{\rho_l}} \tag{6}$$

$$\dot{m}^- = F_{cond}\frac{3\alpha_v \rho_v}{R_{nuc}}\sqrt{\frac{2}{3}\frac{\max(p - p_v, 0)}{\rho_l}} \tag{7}$$

In the formula, F_{vap} and F_{cond} are empirical coefficients of the mass transfer process and are recommended to be 50 and 0.01; Ref. [30] r_{nuc} is the volume fraction of gas core of 5×10^{-4}; and R_{nuc} is a bubble radius of 1×10^{-6} m. p_v is the gasification pressure, Pa. According to the experimental data [30], these parameters of the cavitation model

were discussed and verified. It is successfully applied to the numerical simulation of the cavitation flow in the pump [31].

3.5. Calculation Method and Boundary Conditions

The complex three-dimensional cavitation flow in the water-jet pump is calculated with the commercial software Ansys CFX. The liquid phase is water at 25 °C, the density is 997 kg/m^3, and the kinematic viscosity is 8.899×10^{-4} kgm^{-1}s^{-1}. The SST k-ω turbulence model is adopted. When the cavitation occurs, the vapor phase selects 25 °C water vapor, the density is 0.02308 kg/m^3, and the dynamic viscosity is 9.8626×10^{-6} kgm^{-1}s^{-1}. When the RMS residual is less than 10^{-5}, the calculation stops. Monitor hydraulic head and efficiency until their values are constant. The boundary condition of the inlet is set as pressure inlet. The boundary condition of the outlet is set as mass outflow. Wall boundary conditions uses the non-slip wall. The impeller calculation domain is set to operate at 1450 r/min. The blade and hub are arranged to rotate, the shroud wall speed is set to the counter rotating wall. The diffuser, suction, and outpipe are set to rest. The interface between the rotating part and the stationary part is set to the Frozen Rotor Interface. Figure 6 shows the setting of some special boundary conditions in the CFD setup.
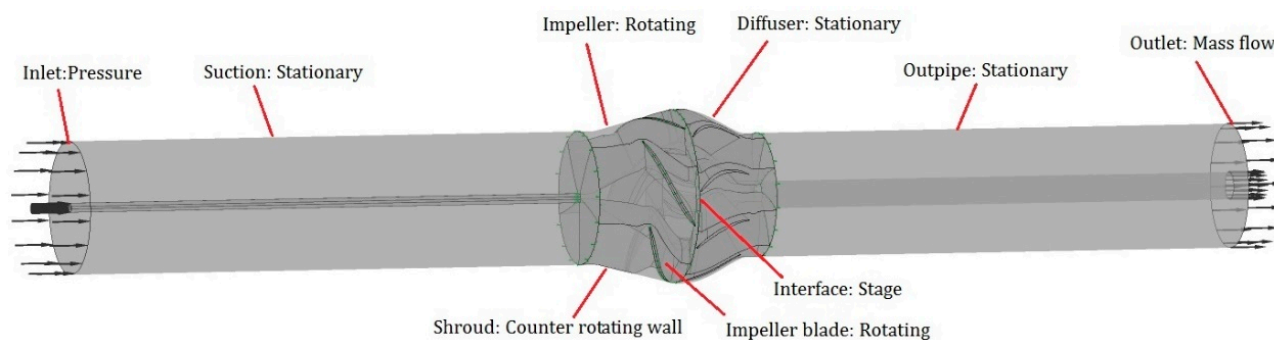

Figure 6. CFD setting.

4. Analysis of Results

4.1. Cavitation Performance Test

Under standard working conditions, the comparison of cavitation performance curves between experimental and numerical simulations of a water-jet pump is shown in Figure 7. When comparing the cavitation performance curves of experiment and numerical simulations, it is found that there are some differences between the two curves; however, the general trend is the same, which can verify the reliability of numerical simulation. Keep the flow constant and gradually reduce the inlet pressure until cavitation occurs and develops. As can be seen from the figure, the head of the pump at point A remains almost constant at the beginning. Although the cavitation phenomenon in the tip of the blade can be seen visually, it is generally believed that cavitation will not occur at this point, so the pump's performance will not be affected at this time. Traditionally, this point is still defined as a non-cavitation condition. When the inlet pressure is gradually reduced, the head curve changes accordingly, and the cavitation of the pump gradually begins to develop. The point B on the cavitation performance curve is called the Initial Cavitation Condition. With the decrease in inlet pressure, the head rises slightly and then tends to drop sharply. Point C on the cavitation performance curve is called the First Critical Cavitation Condition [32]. As the inlet pressure continues to decrease, the head curve drops sharply. When the head drops to 3%, point D on the cavitation performance curve is called the Critical Caving Condition. With the further decrease in inlet pressure, the cavitation performance curve starts to drop sharply, and point E on the cavitation performance curve is called the Breakdown Cavitation Condition. The A~E was selected from the cavitation performance curve of the simulation to mark cavitation conditions, corresponding to the A~E in the cavitation performance curve of experiment.
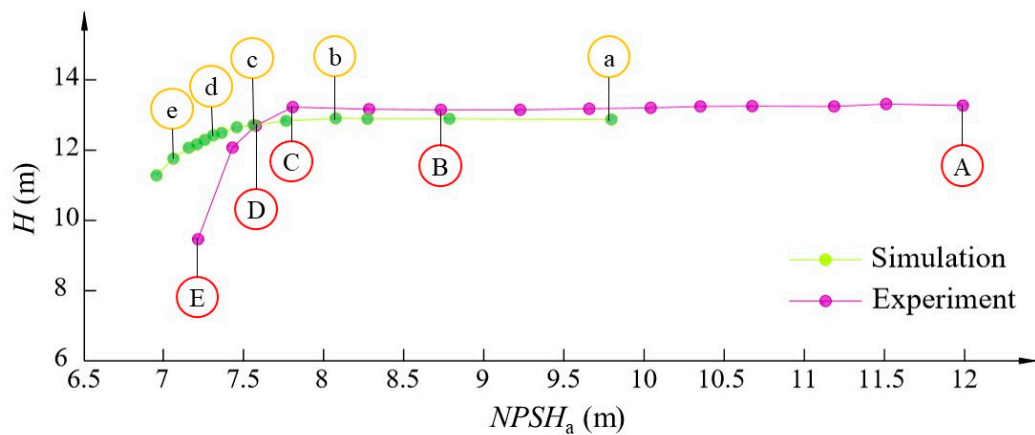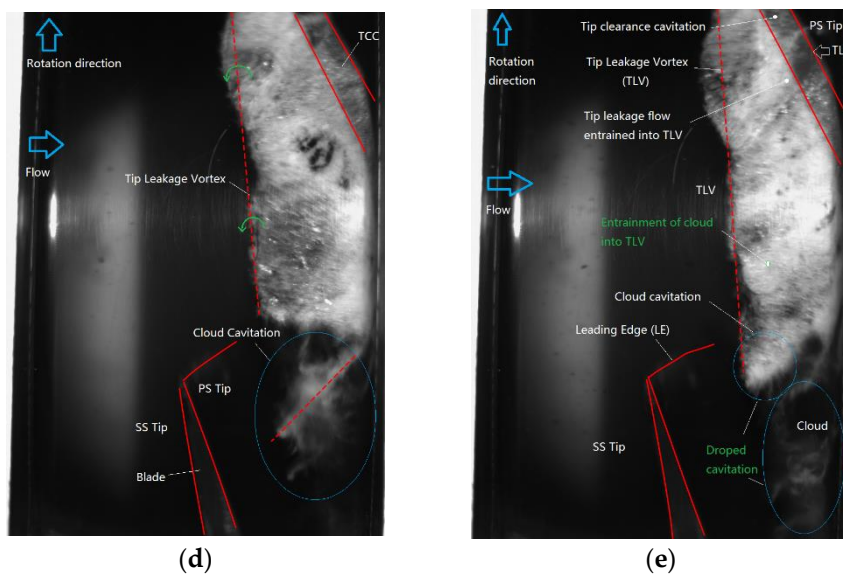
Figure 7. Cavitation flow structure numerical calculation and experimental comparison conditions [28].

Figure 8 shows the cavitation flow structures at different cavitation developments of points A–E in Figure 7. It can be seen that with the decrease of $NPSH_a$, cavity production increases gradually. Figure 8a shows the cavitation flow structures at the Non-Cavitation Condition (point A on the cavitation curve in Figure 7). It can be seen from the figure that, although the performance curve of the pump shown in Figure 4 has not changed, tip vortex cavitation in the tip region is still observed. There are no bubbles appearing on the pressure surface of the blade, and the pressure surface of the adjacent blade is less affected by the Tip Leakage Vortex Cavitation (TLVC). In Figure 8b, the cavitation is more intense than at point A. It can be seen that a triangular cloud cavitation structure is formed in the region between the suction surface and the Tip Leakage Vortex boundary. With the cavitation development, the cloud cavitation begins to fall into large pieces of bubbles. In Figure 8c, the cavitation region is further developed and has almost reached the pressure surface of the impeller blade. The trailing of the triangular zone extended toward the main flow direction, and the scale of shedding cavitation at the trailing of the triangular zone was larger than point B. As shown in Figure 8d, there are much more and larger bubbles appearing in the entrained Tip Leakage Vortex relative to the cavitation state at point D. In Figure 8e, the shedding cavitation at the trailing directly collapses on the pressure surface and enters the adjacent blade tip clearance, which promotes and induces the occurrence and development of cavitation in the adjacent blade. It causes the head of the water to plummet.


(a)

(b)

(c)

Figure 8. *Cont.*

(**d**)   (**e**)
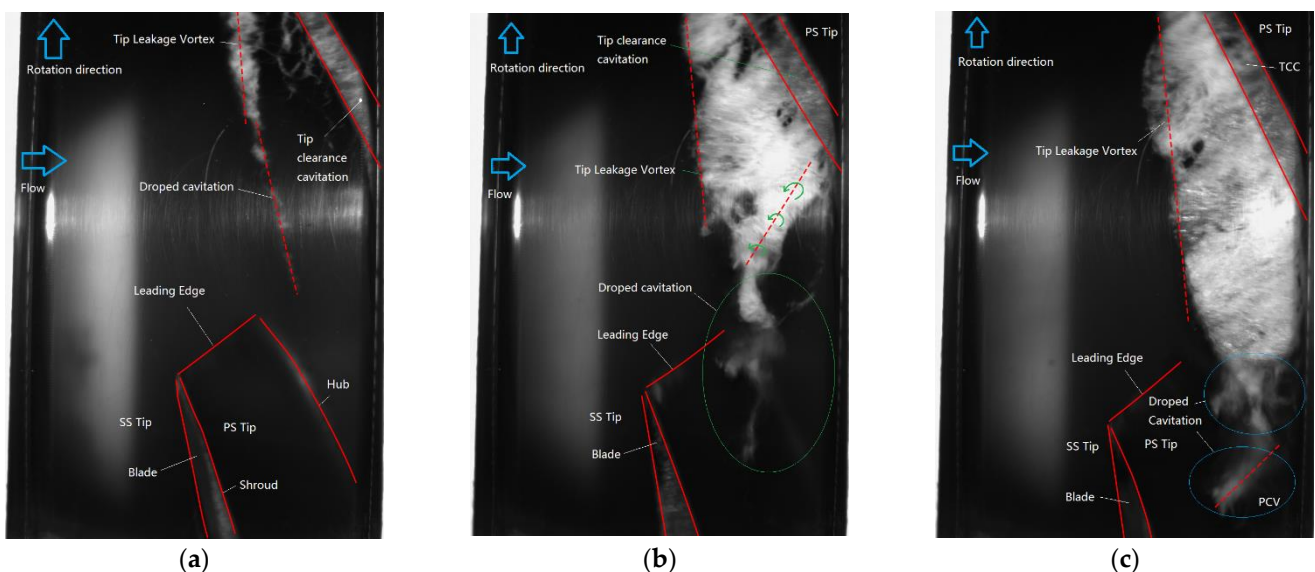
Figure 8. The cavitation flow structures at different cavitation developments [28]. (**a**) Point A, (**b**) point B, (**c**) point C, (**d**) point D, and (**e**) point E.

4.2. Analysis of the Vapor Fraction at Different Cavitation Conditions

Through numerical calculation of the cavitation model, the relationship curve between head H (m), vapor fraction VF (%), and $NPSH$a of the suction surface of the impeller blade in the process of cavitation development is obtained, as shown in Figure 9. It can be seen from Figure 9 that with the reduction of $NPSH$a, the $NPSH$a-H curve first remains constant, then slowly decreases, and then drops sharply after reaching the First Critical Cavitation Condition. Between the Initial Cavitation Condition and the First Critical Cavitation Condition, the $NPSH$a-H curve has shown a slow downward trend, indicating that cavitation is gradually forming and has a certain influence on the pressure surface of the impeller blade. The $NPSH$a-VF curve starts to rise slowly and then rises sharply when the Initial Cavitation Condition is reached. This is mainly because, under the Initial Cavitation Condition, the suction surface of the impeller blade has gathered a part of the cavity and the cloud cavitation has collapsed before reaching the pressure surface.
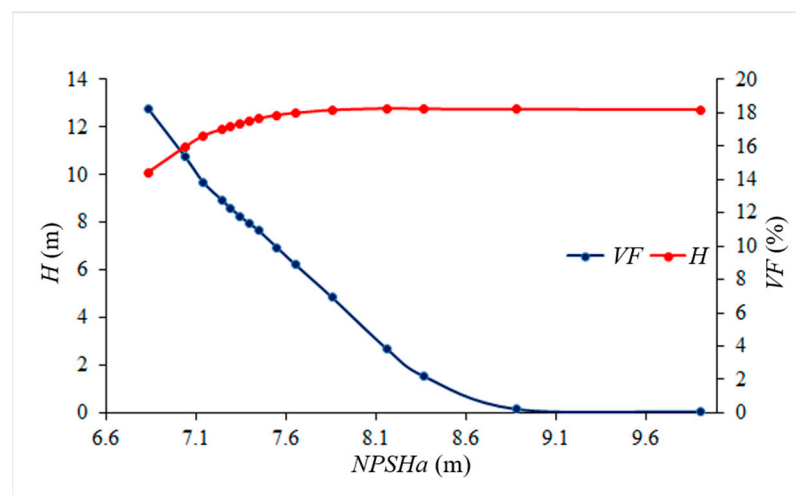
Figure 9. The VF of the impeller blade surface.

Figure 10 shows the cavitation region distribution of the suction surface of the impeller blade under different cavitation conditions. As can be seen from Figure 10, with the decrease of $NPSH$a, the cavitation area shows a gradual expansion trend, indicating that

the cavitation phenomenon in the water-jet pump is gradually becoming serious. With the continuous development of the cavitation phenomenon, the cavitation area gradually extends in the direction of the impeller hub. When cavitation has not yet occurred, there is no obvious bubble on the suction surface of the impeller blade. When the Initial Cavitation Condition is reached, a cavitation area is formed at the suction surface of the impeller blade near the impeller shroud (that is near TLVC). With the continuous development of cavitation, the area of the cavitation area gradually increases. When the Breakdown Cavitation Condition is reached, the cavitation area is most obvious at the suction surface of the impeller blade near the impeller shroud and the impeller TE. Comparing Figure 10 with Figure 8, it is found that the evolution process of the cavitation region on the suction surface of the impeller blade is basically consistent. When *NPSH*a = 6.54 m, near the suction surface TE of the impeller blade, the VF is very high. It is judged that a strong eddy current is formed here, which leads to the cavitation falling off of the suction surface.
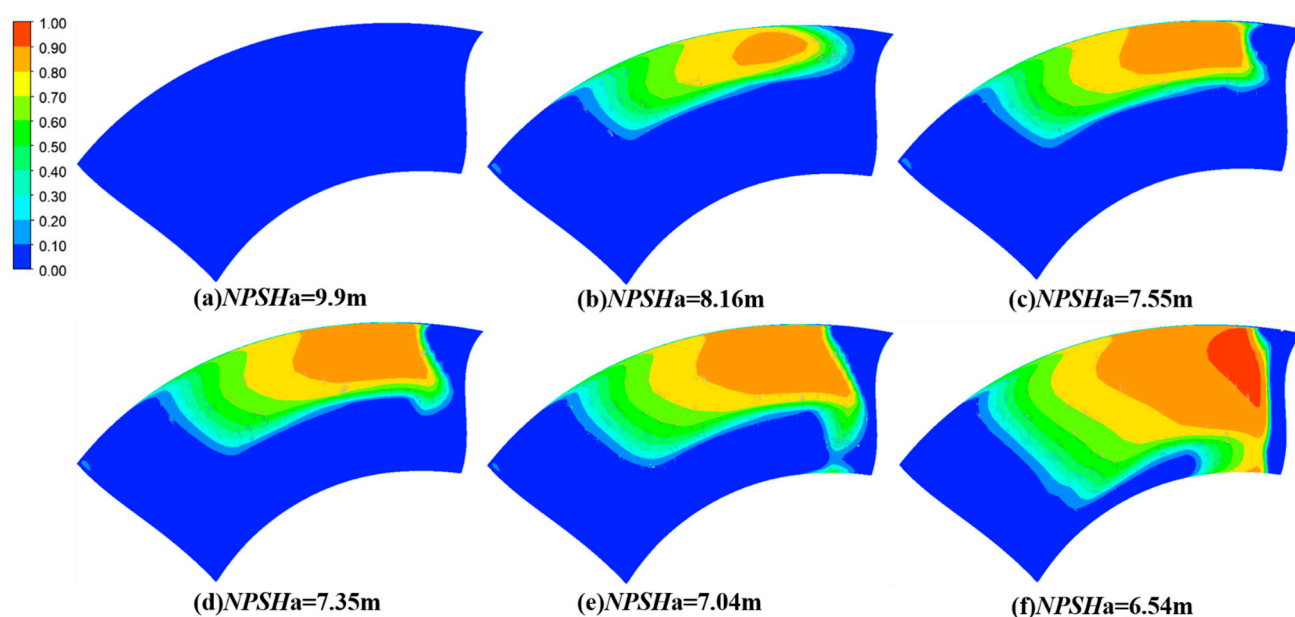
Figure 10. The distribution of the cavitation region of the impeller suction surface under different cavitation conditions.

5. Study on Cavitation Wake Vortex

5.1. The TLV and Separation Vortex

Figure 11 shows the streamline distribution of the suction surface of the impeller blade under different cavitation conditions. Comparing streamlines under different cavitation conditions, it is found that the streamlines are evenly distributed on the suction surface of the impeller blade away from the impeller TE. The velocity on the suction surface of the impeller is relatively high near the shroud of the impeller and gradually decreases as it approaches the hub of the impeller. Under the Non-Cavitation Condition and the Initial Cavitation Condition, the streamline is evenly distributed at the suction surface of the entire impeller blade. Starting from the First Critical Cavitation Condition, at the tip of the impeller TE, that is, near the shroud on the suction surface of the impeller, the streamlines are distorted into a triangular shape, indicating that vortices are formed here. With the development of cavitation, the area of the vortex cluster gradually increases and continues to extend toward the hub of the impeller. After reaching the Breakdown Cavitation Condition, it covers the entire TE on the suction surface of the impeller. Combining Figures 10 and 11, it is found that cavitation is the separation vortex formed by the flow separation in the area near the impeller TE on the suction surface of the impeller blade and the combination of the separation vortex and the TLVC to form the cavitation wake vortex, which leads to the shedding of cavitation.
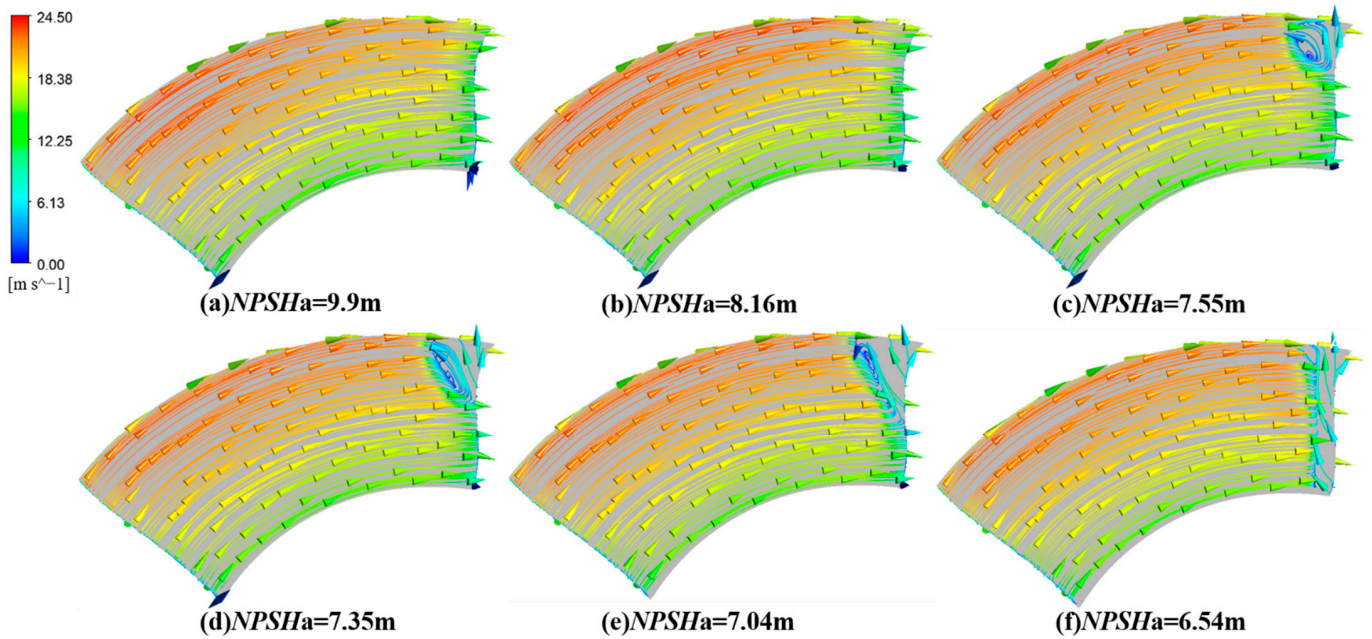
Figure 11. The streamline distribution of the impeller suction surface under different cavitation conditions.

Figure 12 shows the streamline diagram through the impeller tip under different cavitation conditions; Figure 12g is the partially enlarged view of the impeller tip streamline when *NPSH*a = 7.04 m. Due to the effect of the pressure difference, the fluid passes through the suction surface of the impeller blade at high speed from one side of the pressure surface of the impeller blade and flows in the direction of the impeller hub. As the impeller blade rotates, it gradually integrates into the mainstream. It can be seen from the figure that under the Non-Cavitation Condition and the Initial Cavitation Condition, the streamline change at the impeller tip is not obvious. When the First Critical Cavitation Condition is reached, the low-speed vortex cluster will gradually form at the impeller tip near the impeller TE position and gradually expand with the development of cavitation. This also indicates that with the increase of cavitation degree, the cavitation wake vortex formed by the combination of separation vortex and TLVC gradually increases, resulting in the increase of the outer profile of the impeller blade tip streamline.
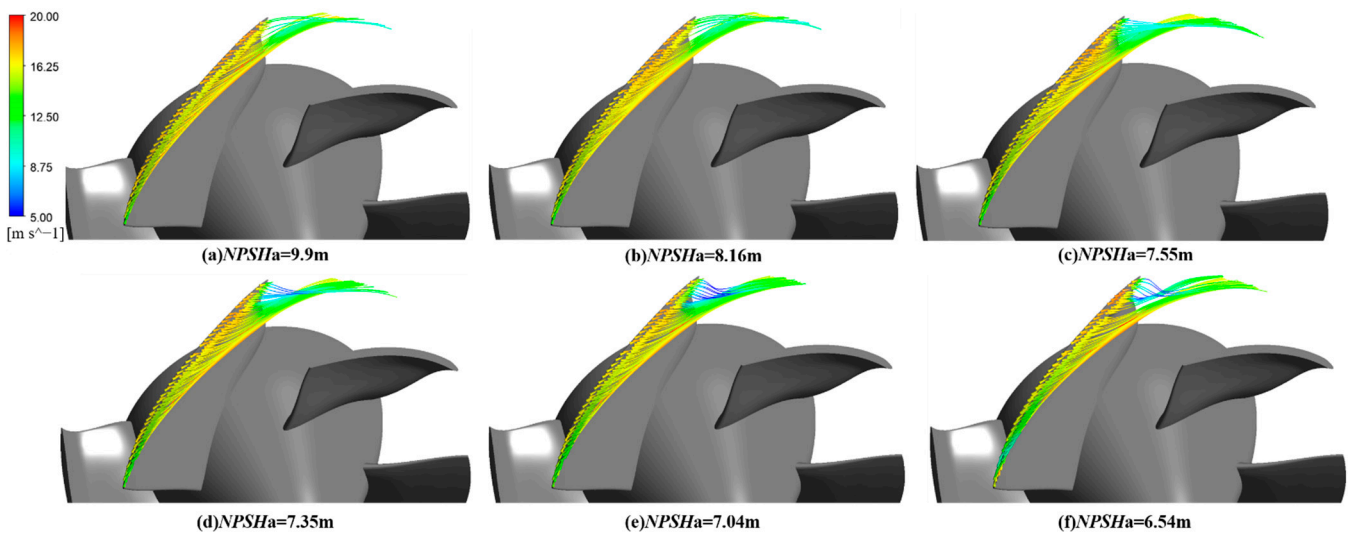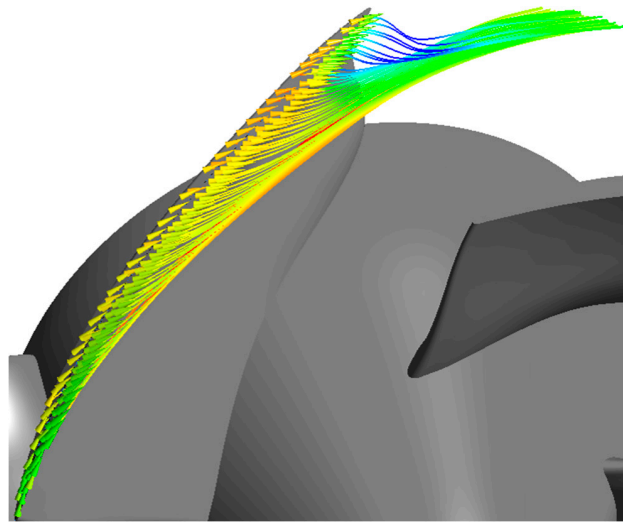

Figure 12. *Cont.*

(g) Partially enlarged view of the impeller tip streamline when *NPSH*a = 7.04m

Figure 12. The streamline diagram through the impeller tip under different cavitation conditions.

5.2. Vorticity Analyze

The vorticity equation can further reveal the vortex characteristics under the influence of cavitation. Considering the Navier–Stokes equation, the vorticity equation of the cavitation flow is as follows [33]:

$$\frac{D\vec{\omega}}{Dt} = \left(\vec{\omega} \cdot \nabla\right)\vec{u} - \vec{\omega}\left(\nabla \cdot \vec{u}\right) + \frac{\nabla\rho_m \times \nabla p}{\rho_m^2} + (\nu_m + \nu_t)\nabla^2\vec{\omega} \tag{8}$$

where $\vec{\omega}$ is the vorticity, $\vec{u}$ is the velocity, ν is the kinematic viscosity, the subscripts of m and t is the mixture phase and turbulent, respectively, and ∇ is Hamiltonian operator. On the right side of Equation (8), each term represents, in turn, the vortex stretching, the vortex dilatation, the barotropic torque, and the viscous diffusion. The Reynolds number is large, its order of magnitude is about 10^6 near the blade tip, and the viscous diffusion term is relatively too small to usually be ignored.

The Z-axis component of the vorticity equation is as follows:

$$\frac{D\vec{\omega}_Z}{Dt} = \left(\left(\vec{\omega} \cdot \nabla\right)\vec{u}\right)_Z - \vec{\omega}_Z\left(\nabla \cdot \vec{u}\right) + \left(\frac{\nabla\rho_m \times \nabla p}{\rho_m^2}\right)_Z + (\nu_m + \nu_t)\nabla^2\vec{\omega}_Z \tag{9}$$

where the variable with the subscripts of Z represents the component of the variable in the Z direction.

Vorticity is the curl of velocity, which is used to describe the rotating motion of fluid microclusters, i.e.,: $\omega = \nabla \times V$. According to the Cauchy–Stokes decomposition, the vorticity is defined as two times of the angular velocity of the fluid pellet when it moves around the center of rotation as a rigid body. The Cauchy–Stokes decomposition is as follows [34]:

$$\nabla V = A + B = \frac{1}{2}(\nabla V + \nabla V^T) + \frac{1}{2}(\nabla V - \nabla V^T) \tag{10}$$

where ∇V is decomposed into symmetric part A and antisymmetric part B, B is the vorticity tensor.

Since the vorticity cannot directly represent the vortex, in order to accurately identify the vortex structure, many scholars have proposed different vortex identification methods, including the Q-criterion, λ_2-criterion, Δ-criterion, etc.

According to the Cauchy–Stokes formula decomposition in formula (10), the second Galilean in the velocity gradient tensor is used Omit invariants to represent vortex structure, the expression of Q can be expressed as [35]:

$$Q = \frac{1}{2}\left(\left\|B\right\|_F^2 - \left\|A\right\|_F^2\right) \tag{11}$$

where $\|\ \|\ \|_F$ is the Frobenius norm of a matrix.

The vortex region is represented by the region Q > 0, which requires that the vortex structure not only contain the antisymmetric tensor B but also that the antisymmetric tensor B can overcome the influence brought by the symmetric tensor A. Compared with other vortex identification methods, Q-criterion has less computation and produces better results. Therefore, the Q-criterion is selected to extract vortex structure.

Figure 13 shows the setting and selection of the plane and the region where cavitation occurs. Figures 14–16 show the contours of the vorticity equation's each term in the Z direction on the section near TE under different cavitation conditions. To facilitate the analysis, the vortex pattern diagram is also shown in those figures. The vortex pattern was identified by the Q-criterion with a level of 0.01. It can be seen that the cavitation region is mainly concentrated near the suction surface of the impeller blade. With the decrease of *NPSH*a, the cavitation region gradually increases, showing the occurrence of cavitation.
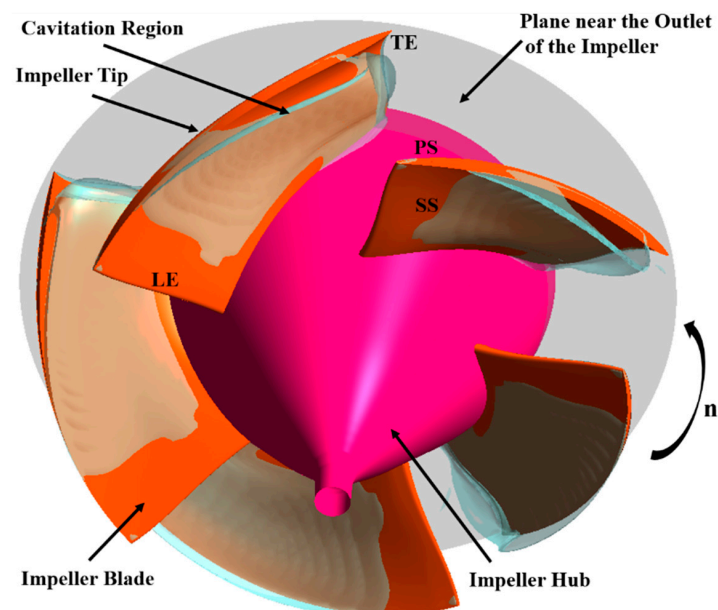
Figure 13. Plane selection and setting.

Figure 14 shows the cavitation region and the contours of the vortex stretching term on the spanwise section near TE. The vortex stretching term mainly reflects the change of vorticity and direction caused by the velocity gradient transformation of the flow field. In Figure 14, the absolute value of vorticity is larger near the tip, close to the shroud. With the gradual occurrence of cavitation, the absolute value of the position of the vortex stretching term on the suction surface of the impeller blade gradually increases. The separation vortex also increases, showing that the velocity gradient generated by flow separation caused by cavitation is gradually increasing. At the same time, it was found that the Tip Leakage Vortex could not be avoided, no matter whether or not the cavitation phenomenon occurred and the degree of its occurrence. However, with the gradual decrease of *NPSH*a, the separation vortices on the suction surface are gradually strengthened, the vortex characteristics after the convergence of TLV and separation vortices are gradually obvious, and the area of the vortex with a larger absolute value is gradually increased in the radial direction. Because the trailing edge of the impeller blade is the intersection of the suction surface and the pressure surface of the blade, a velocity gradient will be generated here.
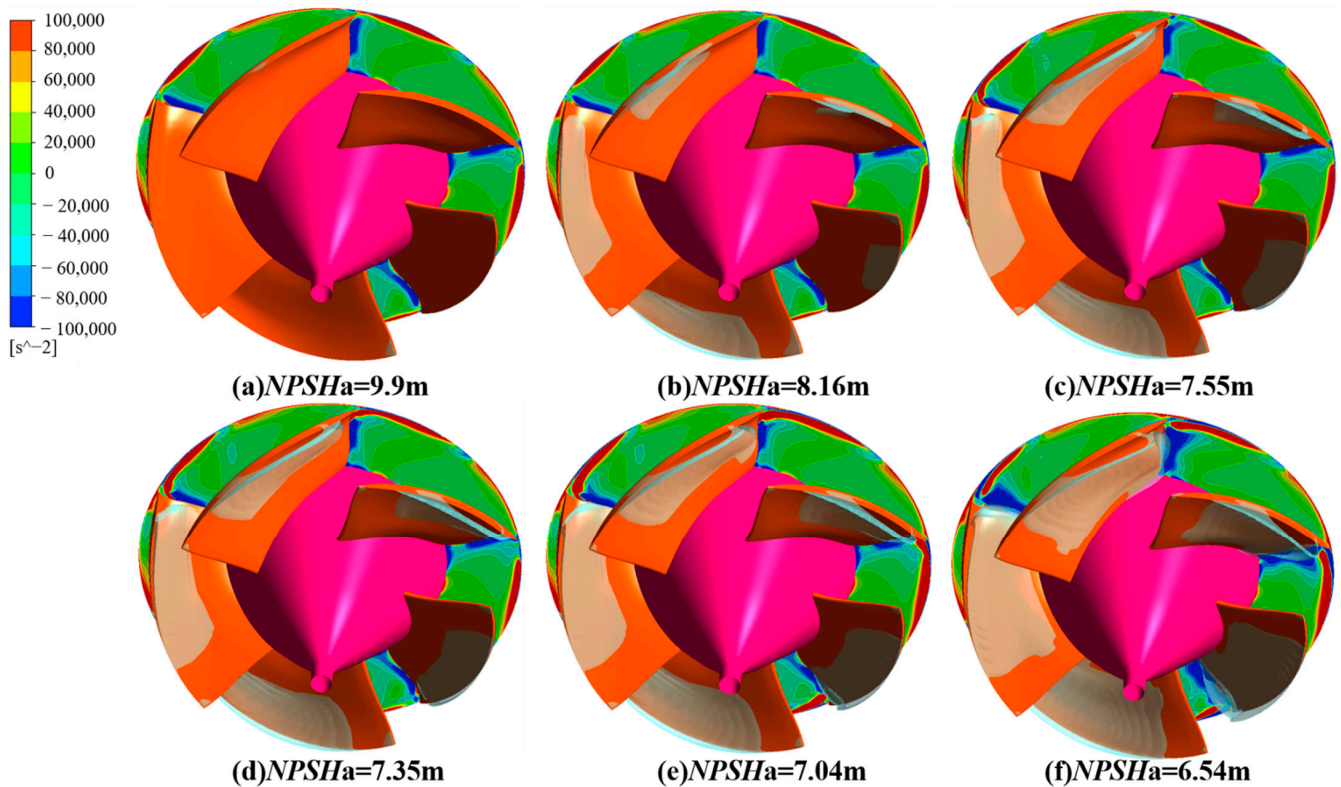
Figure 14. The cavitation region and contours of the vortex stretching term on the spanwise section near TE.

Figure 15 shows the cavitation region and the contours of the vortex dilatation term on the spanwise section near TE. The vortex dilatation term mainly reflects the effect of compressibility of fluid on vorticity. By comparing the isolines under different cavitation conditions, it can be seen that with the increase of the cavitation degree, flow separation on the suction surface gradually increases, and the regional area of vortex dilatation term with a larger absolute value also gradually increases. When *NPSH*a = 7.55 m, the vortex dilatation term with a larger absolute value no longer only adhered to the tip close to the shroud but gradually migrated to TE and the region near the shroud in the impeller runner. After the TLV converged with the separation vortex, the vortex characteristics became more obvious and gradually migrated to the hub direction. In general, the more intense the cavitation is, the higher the vapor volume fraction is, and the stronger the compressibility is. From the figure, it can be seen that the cavity attached to the blade surface contributes more to the dilatation of the vortex than TLVC.

Figure 16 shows the cavitation region and contours of the baroclinic torque term on the spanwise section near TE. As can be seen from Figure 16, under the conditions of Figure 16a,b, the value of the baroclinic torque term is about 0, which is because Figure 16a is in non-cavitation condition, Figure 16b is in a Initial Cavitation Condition, and the reference section is in a non-cavitation region, while the baroclinic torque term mainly plays a role when the pressure gradient and density gradient are inconsistent. Therefore, in the non-cavitation and Initial Cavitation region, the value of the baroclinic torque term is about 0. In Figure 16c, the cloud image near TE was observed on the plane, and it could be found that the value of the baroclinic torque term changed slightly but was still close to 0, which indicated that the pressure gradient and density gradient were basically consistent. In Figure 16d–f, the absolute value of the baroclinic torque term increases gradually with the increase in cavitation degree. The more serious the cavitation, the greater the density gradient of the suction surface of the impeller blade.
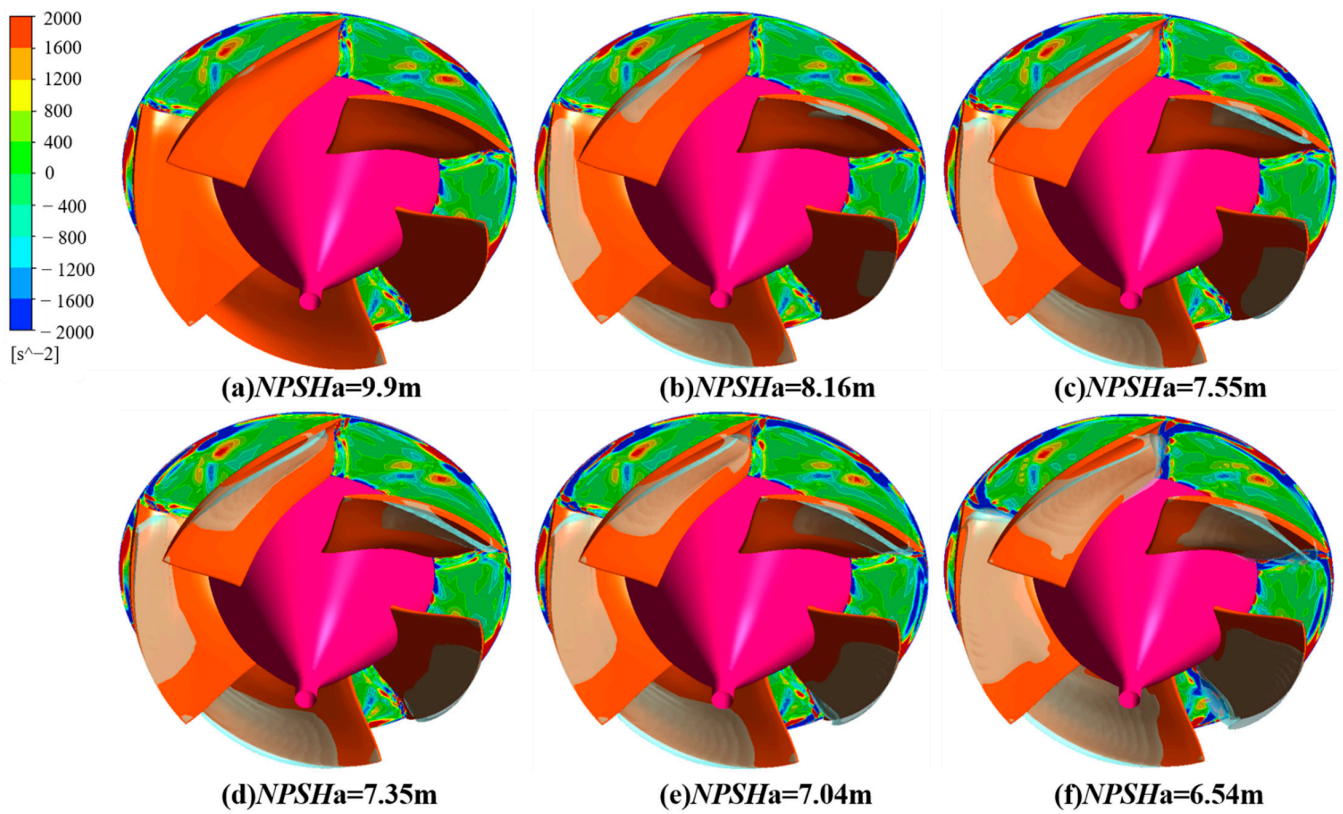
Figure 15. Cavitation region and contours of the vortex dilatation term on the spanwise section near TE.
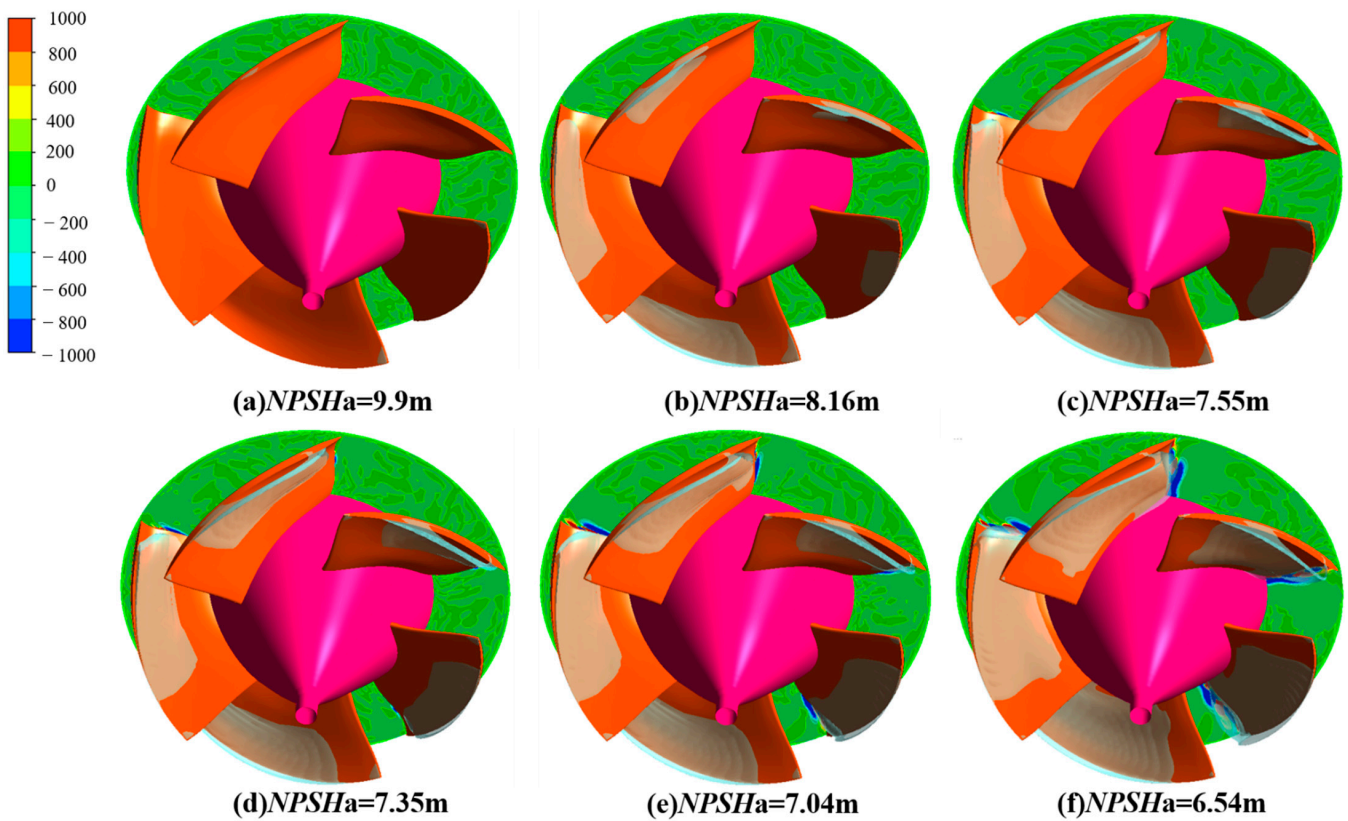

Figure 16. The cavitation region and the contours of the baroclinic torque term on the spanwise section near TE.

The third term of Equation (8) is called the force tube term or baroclinic term, which indicates that pressure-density changes can cause changes in the vorticity vector of the fluid. The physical essence is the baroclinic property of the fluid, and what really causes changes in the vorticity vector of the fluid is the baroclinic property of the fluid.

In order to further reveal the relationship between the cavitation vortex structure on the suction surface of the impeller blade and the density and pressure distribution, three planes were selected to analyze the density and pressure distribution on different planes. Figure 17 shows the selection and setting of the density and the pressure contour plane section under the Breakdown Cavitation Condition. Plane 1 is set at the outlet of the impeller blade, that is, near TE; Plane 2 is set at the end of the cavitation area on the suction surface of the impeller blade; and Plane 3 is set at the middle of the impeller blade.

Figure 18 shows the density distribution contours of three planes under the Breakdown Cavitation Condition. It can be seen that the medium at Plane 1 is mainly water. At Plane 2, there is a certain amount of vapor near the tip of the suction surface of the impeller blade, while at Plane 3, the medium density in the entire impeller flow channel decreases. There is also a certain amount of vapor at the tip of the suction surface of the impeller blade, which extends toward the direction of the impeller hub compared with Figure 18b. It can be seen from Figure 18d that there is an obvious boundary in the density distribution at the outer edge of the flaky cavitation on the blade surface, and the density distribution is very consistent with the cavitation area.

Figure 19 shows the pressure distribution contours of three planes under the Breakdown Cavitation Condition. It can be seen that there is a large pressure at the blade tip where the impeller tip and TE intersect at Plane 1, and the pressure gradually decreases as it approaches the impeller hub. At Plane 2, the pressure at the junction of Plane 2 and the impeller blade is small. Seen from a clockwise direction, the pressure gradually increases. At Plane 3, the low-pressure area at the junction of Plane 3 and the impeller blade is more obvious, but the overall pressure of Plane 3 in the impeller flow channel is lower than that of Plane 2. It can be seen from Figure 19d that there is no obvious relationship between cavitation area and pressure distribution.

Therefore, the density distribution characteristics of the fluid inside the vortex structure can be further analyzed. Because the vortex core is not only the center of the vortex structure but also the lowest point of the fluid density inside the vortex structure, it can be used as the density reference point [36]. However, the relationship between the vortex structure with different spatial dimensions, the growth and annihilation processes of the vortex structure, the change in the geometry of the vortex structure, and the fluid density inside the vortex structure remains to be further studied.
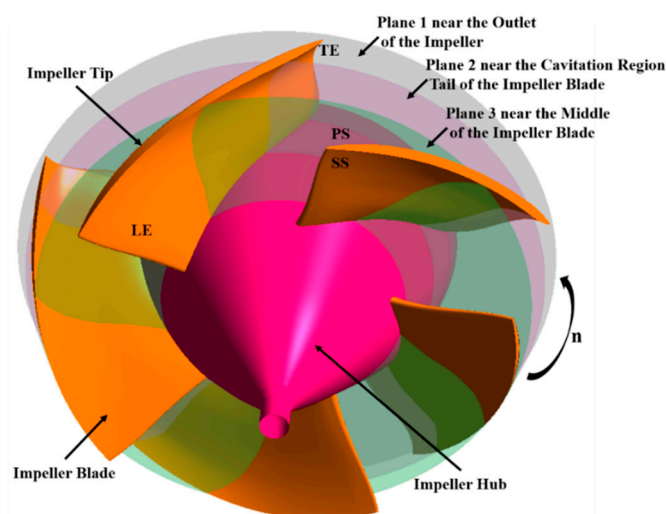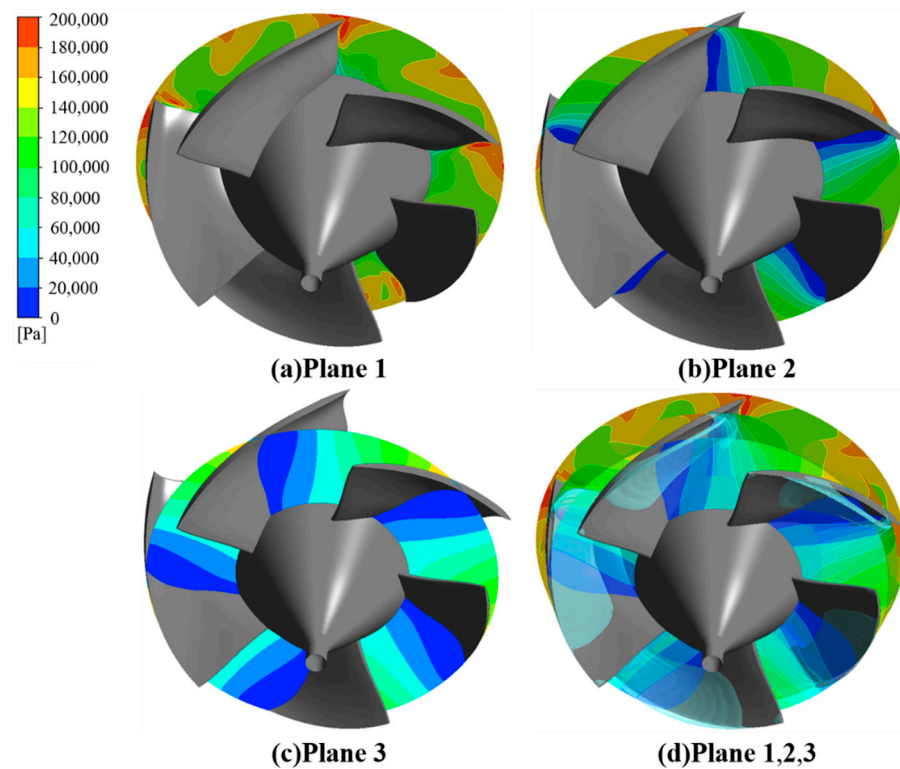

Figure 17. Selection and setting of the density and the pressure contour plane section under the Breakdown Cavitation Condition.
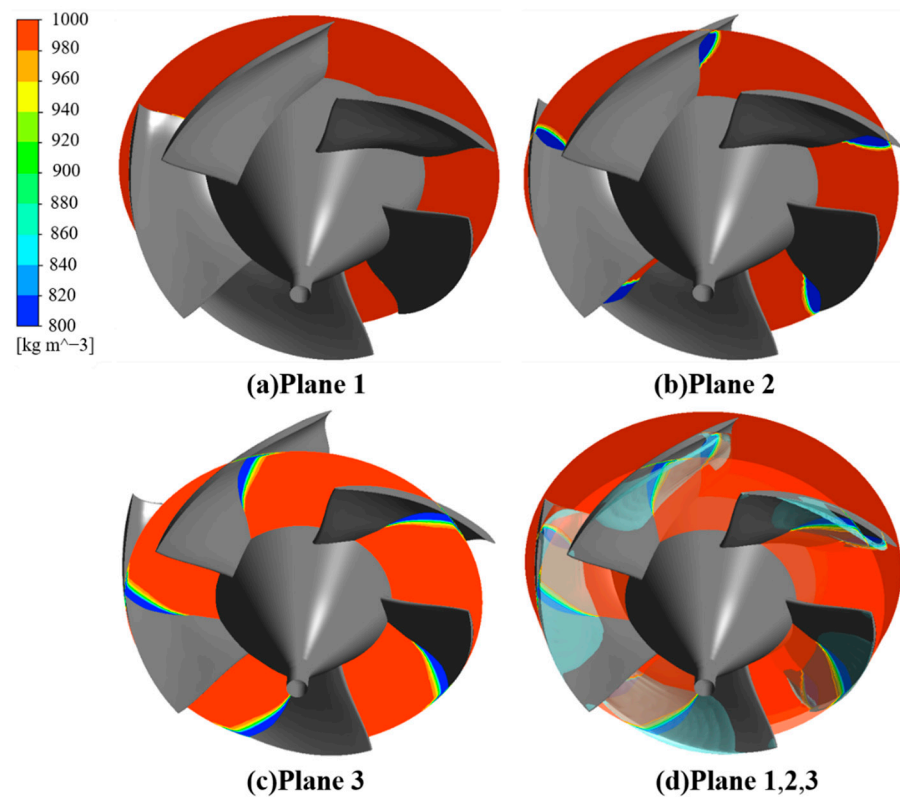
Figure 18. Contours of the density on different planes under the Breakdown Cavitation Condition.

Figure 19. Contours of the pressure on different planes under the Breakdown Cavitation Condition.

5.3. Discussion

Visualization experiments using HSP technology are carried out to capture the complex cavitation flow phenomenon in the pump. However, if conditions permit, a PIV refinement

of the flow field means obtaining the flow field distribution in the pump that cannot be photographed by HSP is still needed, so as to conduct further research. With the decrease of the pump inlet pressure, *NPSH*a gradually decreases, the head curve decreases from gentle to sharp, the cavitation in the pump gradually develops, and the cavity gradually increases until the condition of breakdown cavitation is reached, which seriously affects the performance of the pump. Therefore, how to effectively and simply suppress TLV cavitation is a problem worthy of further discussion.

After reaching the First Critical Cavitation Condition, because the separation vortex converges with TLV at the suction surface of the impeller blade near the impeller shroud and TE, a strong cavitation wake vortex is formed. The area with a large absolute value of the vortex stretching term gradually extends to the direction of the impeller hub. It can be seen from Figure 15 that there is a large negative area on the suction surface of the impeller under the First Critical Cavitation Condition and the Critical Cavitation Condition. With the intensification of cavitation, when the Breakdown Cavitation Condition develops, the negative region disappears while the positive region near the suction surface of the impeller gradually expands. The causal relationship between the disappearance of the negative region and the cavitation rupture needs further study.

The relationship between the cavitation vortex structure on the suction surface of the impeller blade and the density and pressure distribution is revealed. However, the fluid distribution characteristics in the vortex structures under different cavitation conditions need to be studied more.

6. Conclusions

In this paper, the cavitation flow structure and impeller cavitation vortex structure during the development of cavitation are studied by means of both experimental and numerical simulations. The cavitation flow structure in the pump is captured by high-speed photography. The VF on the impeller and the vortex structure of the impeller cavitation wake vortex at different cavitation conditions were analyzed, and the relationship between the cavitation region and the impeller cavitation wake vortex structure was revealed. The main work and conclusions are as follows:

(1) The cavitation performance curve of the water-jet pump at the designed flow rate is obtained. The high-speed photography technology is used to capture the cavitation flow structure under different cavitation conditions at the design flow. Through the HSP visualization test, the cavitation flow state picture in the water-jet pump was clearly obtained, and the cavitation performance curve was obtained. The reliability of the numerical simulation results was verified by comparing them with the numerical simulation results, which provided a reference for the subsequent visualization test research on the cavitation flow in the pump;

(2) The VF inside the impeller and the cavitation distribution region on the impeller suction surface are analyzed under the Non-Cavitation Condition, the Initial Cavitation Condition, the First Critical Cavitation Condition, Critical Cavitation Condition, and the Breakdown Cavitation Condition, respectively. Through the comparative with the distribution of the limit streamline of the suction surface, the formation mechanism of the separation vortex near the TE end of the impeller is revealed;

(3) By identifying the cavitation wake vortex structure, it can be seen that TLV is inevitable, whether cavitation occurs or not. However, with the gradual enhancement of the separation vortex on the impeller suction surface, the vortex characteristics of the TLV after converging with the separation vortex gradually became apparent. This shows that the relative motion between the impeller tip and the shroud and the cavitation region of the suction surface have important effects on the cavitation wake vortex structure. Due to the complexity of the TLV cavitation structure, effective control of TLV cavitation has always been an important and challenging problem in engineering practice and academic research. This paper further advances the research of TLV cavitation, which has practical significance in engineering.

References

1. Pei, J.; Yin, T.; Yuan, S.; Wang, W.; Wang, J. Cavitation optimization for a centrifugal pump impeller by using orthogonal design of experiment. *Chin. J. Mech. Eng.* **2017**, *30*, 103–109. [CrossRef]
2. Long, Y.; Zhang, Y.; Chen, J.; Zhu, R.; Wang, D. A cavitation performance prediction method for pumps: Part 2—Sensitivity and accuracy. *Nucl. Eng. Technol.* **2021**, *53*, 3612–3624. [CrossRef]
3. Long, Y.; Zhu, R.; Wang, D. A cavitation performance prediction method for pumps PART1-Proposal and feasibility. *Nucl. Eng. Technol.* **2020**, *52*, 2471–2478. [CrossRef]
4. Han, C.Z.; Xu, S.; Cheng, H.Y.; Ji, B.; Zhang, Z.Y. LES method of the tip clearance vortex cavitation in a propelling pump with special emphasis on the cavitation-vortex interaction. *J. Hydrodyn.* **2020**, *32*, 1212–1216. [CrossRef]
5. Li, D.; Zhang, N.; Jiang, J.; Gao, B.; Alubokin, A.A.; Zhou, W.; Shi, J. Numerical investigation on the unsteady vortical structure and pressure pulsations of a centrifugal pump with the vaned diffuser. *Int. J. Heat Fluid Flow* **2022**, *98*, 109050. [CrossRef]
6. Zhang, D.S.; Shi, L.; Zhao, R.J.; Shi, W.D.; Pan, Q.; van Esch, B. Study on unsteady tip leakage vortex cavitation in an axial-flow pump using an improved filter-based model. *J. Mech. Sci. Technol.* **2017**, *31*, 659–667. [CrossRef]
7. Li, Y.; Feng, G.; Li, X.; Si, Q.; Zhu, Z. An experimental study on the cavitation vibration characteristics of a centrifugal pump at normal flow rate. *J. Mech. Sci. Technol.* **2018**, *32*, 4711–4720. [CrossRef]
8. Azizi, R.; Hajnayeb, A.; Ghanbarzadeh, A.; Changizian, M. Cavitation Severity Detection in Centrifugal Pumps. In Proceedings of the Advances in Technical Diagnostics, Gliwice, Poland, 12–16 September 2018; pp. 47–55.
9. Ge, M.; Sun, C.; Zhang, X.; Coutier-Delgosha, O.; Zhang, G. Synchrotron X-ray based particle image velocimetry to measure multiphase streamflow and densitometry. *Radiat. Phys. Chem.* **2022**, *200*, 110395. [CrossRef]
10. Lu, J.; Yuan, S.; Luo, Y.; Yuan, J.; Zhou, B.; Sun, H. Numerical and experimental investigation on the development of cavitation in a centrifugal pump. *Proc. Inst. Mech. Eng. Part E-J. Process Mech. Eng.* **2016**, *230*, 171–182. [CrossRef]
11. Liu, M.; Zhou, L.J.; Wang, Z.W. Numerical investigation of the cavitation instability in a central jet pump with a large area ratio at normal cavitating conditions. *Int. J. Multiph. Flow* **2019**, *116*, 153–163. [CrossRef]
12. Al-Obaidi, A.R. Investigation of effect of pump rotational speed on performance and detection of cavitation within a centrifugal pump using vibration analysis. *Heliyon* **2019**, *5*, e01910. [CrossRef] [PubMed]
13. Xu, W.H.; He, X.K.; Hou, X.; Huang, Z.H.; Wang, W.S. Influence of wall roughness on cavitation performance of centrifugal pump. *J. Braz. Soc. Mech. Sci. Eng.* **2021**, *43*, 314. [CrossRef]
14. Ge, M.; Petkovsek, M.; Zhang, G.; Jacobs, D.; Coutier-Delgosha, O. Cavitation dynamics and thermodynamic effects at elevated temperatures in a small Venturi channel. *Int. J. Heat Mass Transf.* **2021**, *170*, 120970. [CrossRef]
15. Ge, M.; Manikkam, P.; Ghossein, J.; Subramanian, R.K.; Coutier-Delgosha, O.; Zhang, G. Dynamic mode decomposition to classify cavitating flow regimes induced by thermodynamic effects. *Energy* **2022**, *254*, 124426. [CrossRef]
16. Ge, M.; Sun, C.; Zhang, G.; Coutier-Delgosha, O.; Fan, D. Combined suppression effects on hydrodynamic cavitation performance in Venturi-type reactor for process intensification. *Ultrason. Sonochem.* **2022**, *86*, 106035. [CrossRef] [PubMed]
17. Ge, M.; Zhang, G.; Petkovsek, M.; Long, K.; Coutier-Delgosha, O. Intensity and regimes changing of hydrodynamic cavitation considering temperature effects. *J. Clean. Prod.* **2022**, *338*, 130470. [CrossRef]
18. Zhang, N.; Gao, B.; Li, Z.; Ni, D.; Jiang, Q. Unsteady flow structure and its evolution in a low specific speed centrifugal pump measured by PIV. *Exp. Therm. Fluid Sci.* **2018**, *97*, 133–144. [CrossRef]
19. Zhang, N.; Liu, X.; Gao, B.; Xia, B. DDES analysis of the unsteady wake flow and its evolution of a centrifugal pump. *Renew. Energy* **2019**, *141*, 570–582. [CrossRef]
20. Zhang, N.; Liu, X.K.; Gao, B.; Wang, X.J.; Xia, B. Effects of modifying the blade trailing edge profile on unsteady pressure pulsations and flow structures in a centrifugal pump. *Int. J. Heat Fluid Flow* **2019**, *75*, 227–238. [CrossRef]
21. Liu, D.M.; Xu, W.L.; Zhao, Y.Z. Experimental study of the flow field of a high head model pump turbine based on PIV technique. *J. Hydrodyn.* **2021**, *33*, 1045–1055. [CrossRef]

22. Shi, B.C.; Xue, K.; Pan, J.P.; Zhang, X.K.; Ying, R.M.; Wu, L.J.; Zhang, Y.D. Liquid/solid flow field in a centrifugal pump with different impeller blade types by PIV. *Meas. Control* **2021**, *54*, 1219–1233. [CrossRef]
23. Shi, B.C.; Wei, J.J.; Zhang, Y. A novel experimental facility for measuring internal flow of Solid-liquid two-phase flow in a centrifugal pump by PIV. *Int. J. Multiph. Flow* **2017**, *89*, 266–276. [CrossRef]
24. Wang, Z.N.; Jin, Y.P.; Huang, F. Investigation of the inner structure of gas-liquid flow in airlift pumps by laser-high speed visualization technology. *Asia-Pac. J. Chem. Eng.* **2020**, *15*, e2509. [CrossRef]
25. Deng, W.Q.; Li, Z.; Ji, L.; Shang, L.M.; Liu, D.M.; Liu, X.B. Laser Doppler Velocimetry Test of Flow Characteristics in Draft Tube of Model Pump Turbine. *Processes* **2022**, *10*, 1323. [CrossRef]
26. Zhu, B.; Chen, H.; Wei, Q. Numerical and Experimental Investigation of Cavitating Characteristics in Centrifugal Pump with Gap Impeller. *Int. J. Turbo Jet-Engines* **2014**, *31*, 187–196. [CrossRef]
27. Shao, C.; Gu, B.; Zhou, J.; Cheng, W. Internal flow measurement in centrifugal pump by high speed photography and error analysis. *Trans. Chin. Soc. Agric. Eng.* **2015**, *31*, 52–58.
28. Long, Y.; An, C.; Zhu, R.S.; Chen, J.P. Research on hydrodynamics of high velocity regions in a water-jet pump based on experimental and numerical calculations at different cavitation conditions. *Phys. Fluids* **2021**, *33*, 045124. [CrossRef]
29. Huang, R.; Ji, B.; Luo, X.; Zhai, Z.; Zhou, J. Numerical investigation of cavitation-vortex interaction in a mixed-flow waterjet pump. *J. Mech. Sci. Technol.* **2015**, *29*, 3707–3716. [CrossRef]
30. Zwart, P.; Gerber, A.G.; Belamri, T. A two-phase flow model for predicting cavitation dynamics. In Proceedings of the Fifth International Conference on Multiphase Flow, Yokohama, Japan, 30 May 2004.
31. Luo, X.; Wei, W.; Ji, B.; Pan, Z.; Zhou, W.; Xu, H. Comparison of cavitation prediction for a centrifugal pump with or without volute casing. *J. Mech. Sci. Technol.* **2013**, *27*, 1643–1648. [CrossRef]
32. Pan, Z.; Yuan, S. *Fundamentals of Cavitation in Pumps*; Jiangsu University Press: Zhenjiang, China, 2013. (In Chinese)
33. Yu, Z. *Numerical and Physical Investigation of Tip Leakage Vortex Cavitating Flows*; Beijing Institute of Technology: Beijing, China, 2016.
34. Shun, X. Investigation on the Mechanism between Vortex and Cavitation in Propelling Pump Tip Clearance with Front Guide Vanes. Ph.D. Thesis, Wuhan University, Wuhan, China, 2020. (In Chinese).
35. Hunt, J.; Wray, A.; Moin, P. Eddies, streams, and convergence zones in turbulent flows. *Stud. Turbul. Using Numer. Simul. Databases* **1988**, *1*, 193–208.
36. Guangming, G.; Lin, Z.; Boyang, X. Density distribution characteristics of fluid in supersonic mixing layer vortex structure. *Acta Phys. Sin.* **2020**, *69*, 126–140. (In Chinese)